

Effects of Multiple-Bond Ruptures on Kinetic Parameters Extracted from Force Spectroscopy Measurements: Revisiting Biotin-Streptavidin Interactions

Senli Guo, Chad Ray, Andrea Kirkpatrick, Nimit Lad, and Boris B. Akhremitchev

Department of Chemistry, Duke University, Durham, North Carolina 27708

ABSTRACT Force spectroscopy measurements of the rupture of the molecular bond between biotin and streptavidin often results in a wide distribution of rupture forces. We attribute the long tail of high rupture forces to the nearly simultaneous rupture of more than one molecular bond. To decrease the number of possible bonds, we employed hydrophilic polymeric tethers to attach biotin molecules to the atomic force microscope probe. It is shown that the measured distributions of rupture forces still contain high forces that cannot be described by the forced dissociation from a deep potential well. We employed a recently developed analytical model of simultaneous rupture of two bonds connected by polymer tethers with uneven length to fit the measured distributions. The resulting kinetic parameters agree with the energy landscape predicted by molecular dynamics simulations. It is demonstrated that when more than one molecular bond might rupture during the pulling measurements there is a noise-limited range of probe velocities where the kinetic parameters measured by force spectroscopy correspond to the true energy landscape. Outside this range of velocities, the kinetic parameters extracted by using the standard most probable force approach might be interpreted as artificial energy barriers that are not present in the actual energy landscape. Factors that affect the range of useful velocities are discussed.

INTRODUCTION

Molecular bonds that mediate cellular structural stability, adhesion, and mobility as well as the function of molecular motors and other specialized cellular components are often subjected to external forces (1–3). These external forces bias the energy landscape of molecular bonds, with sufficiently high forces noticeably altering the bond lifetime (1,4). If the direction of applied force approximately coincides with a separation coordinate between molecules, the applied bias lowers the activation energy, thus increasing the dissociation rate (4–6). Models that consider the time-dependent tilting of the potential of mean force (PMF) quantitatively explain variations in the statistics of rupture forces under dynamic loading (7–13). On the other hand, the investigation of molecular bond rupture under an applied force provides valuable kinetic information for a dissociation reaction not available from other techniques (9). This concept is used in force spectroscopy to uncover details of the energy landscapes that govern bonds between biological molecules (4,14–16).

Single-molecule force spectroscopy is becoming a widespread approach in biophysical research. This technique has been used to characterize conformational transitions of biomacromolecules (17–20) and to quantify the energy landscape in a wide range of molecular associations including ligand-receptor interactions (16,21), complementary DNA strand interactions (22–24), antibody-antigen interactions

(25,26), nonspecific interactions between amyloidogenic peptides (27,28), and hydrophobic interactions (29). Force spectroscopy measurements are performed by directly probing the intermolecular potential with an external mechanical load and registering either the conformational transitions or the ruptures of molecular bonds (16,30,31). Here, we consider the rupture-force modality of force spectroscopy experiments. The measured rupture forces and the force loading rates are used to extract kinetic parameters of molecular interactions. Specifically, the dissociation rates at zero force, the distance to the activation barrier, and the activation energy are quantified by applying appropriate theoretical models (4,9,12,32–34).

Theoretical models that are typically used in the data analysis imply that only one bond dissociates during a given rupture event. However, because of the probe's finite size and the nonzero grafting density, formation of multiple bonds during the tip-sample contact is possible. If the tethers connecting two (or more) separate bonds are relatively close in length, the ruptures of these bonds might occur nearly simultaneously during one rupture event. In this case the measured rupture force is initially distributed between different bonds and the net force is likely to exceed the rupture force of the individual bond. In a significant majority of force spectroscopy experiments, the grafting density is not precisely controlled. Therefore, if there is no additional criteria indicating that only one molecular bond is being studied (such as the "signature" pattern in the unfolding of tandem protein repeats (35)), some contribution of multiple-bond ruptures to the set of measured rupture forces might be expected. Sometimes the measured distribution of rupture

Submitted March 20, 2008, and accepted for publication June 19, 2008.

Address reprint requests to Boris B. Akhremitchev, Tel.: 919-660-1648; Fax: 919-660-1605; E-mail: boris.a@duke.edu.

Andrea Kirkpatrick's present address is Division of Chemistry and Chemical Engineering, California Institute of Technology, Pasadena, CA 91125.

Editor: Peter Hinterdorfer.

forces is very wide and the presence of multiple-bond ruptures is readily apparent (21,36–38). Most theories of multiple parallel bond ruptures assume that the force is distributed evenly between different bonds (37–40). However, it is likely that in real experiments force distribution is uneven.

The uneven distribution of forces originates from tether polydispersity, difference in the tether attachment positions along the probe, and from sample roughness (39,40). As a consequence, one bond will experience higher loading force than the other bonds, as illustrated in Fig. 1. The bond experiencing higher force has a higher probability of rupturing first. Upon the first bond rupture, a part of the total force will be immediately transferred to the second bond and it may rupture during the same rupture event. This rupture event will occur when the total force is significantly below an integer multiple of a single-bond rupture force. Consequently, the peak in the distribution of rupture forces corresponding to the rupture of two independent bonds might significantly overlap with the peak of a single-bond rupture. Recently, an analytical model describing the simultaneous rupture of two independent bonds loaded by tethers of different length was introduced (41). Others have considered ruptures of multiple bonds connected by tethers of uneven length (42). However, it is still assumed that the forces are distributed evenly between different bonds in the model (42). This particular case is incorporated into a new model in the limit of the same tether lengths (41). The new model was applied to study nonspecific pairwise interactions between fullerenes in water using samples that were prepared with increasing grafting density. The two-bond model confirms the sublinear additivity of rupture forces and allows separation of the single-

and double-bond contributions in the distribution of rupture forces. This separation facilitates the extraction of kinetic parameters that are not biased by the presence of multiple-bond ruptures (41).

Here, the two-bond rupture model is applied to analyze the rupture experiments between biotin and streptavidin. The biotin-streptavidin system is a ligand-receptor system that is well studied by force spectroscopy because of the high affinity and specificity of the interaction (16,21,37,43–49). Experimental investigation of the biotin-streptavidin interaction is particularly attractive because molecular dynamics simulations predict a PMF with two very distinct energy barriers (4,50). Although the binding of biotin to streptavidin has been extensively studied by force spectroscopy, quantitative matching of the energy landscape obtained from simulation and from measurements is still problematic. As indicated below, the measurements often place the transition barriers much closer to the equilibrium position than predicted by the simulation. In our opinion, this difference comes in part from neglecting the multiple-bond ruptures that are likely to occur in experimental measurements. We suggest that the previously measured broad distributions of rupture forces with a tail or shoulder on the high-force side of the distribution (21,44,46,47) is a manifestation of the multiple-bond ruptures. Each streptavidin molecule can bind four biotin molecules, and this multiple valence increases the probability of forming multiple bonds during the measurements. Other proposed explanations of the high rupture forces (47,51) are considered below in the Discussion section.

Our experiments use the atomic force microscopy (AFM) approach to perform force spectroscopy measurements. AFM uses relatively sharp probes with a typical radius of curvature of 10–50 nm. The size of these probes does not guarantee that only one bond will be formed during the tip-sample contact. We attempt to decrease the possible number of bonds formed during the tip-sample contact by incorporating water-soluble polymeric tethers to covalently attach biotin molecules to the AFM probes. By employing relatively long tethers (contour length ~ 30 nm), the specific ruptures of the biotin-streptavidin bond can be easily distinguished from nonspecific adhesion between the tip and the substrate surface. This sample preparation approach provides a narrower distribution of rupture forces when compared to some distributions from previous measurements (44,48). However, the width of the measured distributions points to the possibility of multiple-bond ruptures, though it is sufficiently narrow to confine the majority of the measured forces to the limits of the two-bond model.

The two-bond analytical model does not assume any specific shape of the PMF (41). It can be used with different models that describe the dissociation rate dependence on the applied force. The dissociation rate dependence on force can be computed numerically for a given PMF (52,53). However this approach requires a priori selection of a particular shape of a potential and the determination of a set of fitting parameters that is not obvious. Using analytical kinetic models

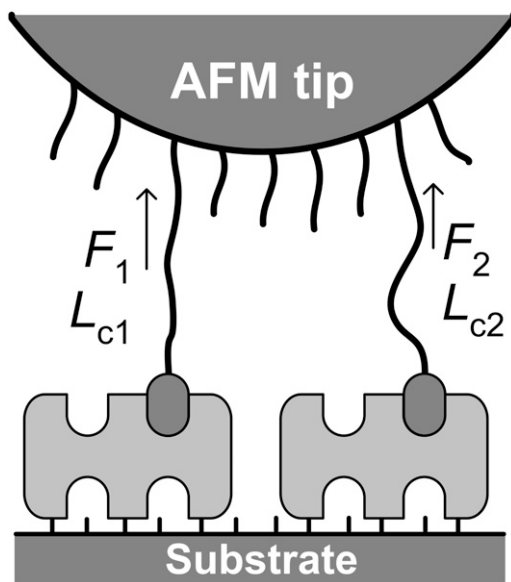


FIGURE 1 Schematic diagram of the rupture of two parallel tethered biotin molecules from streptavidin.

(4,9–12,54,55) simplifies the data analysis and significantly reduces the data processing time. The empirical Bell-Evans model (1,4) is often used in the rupture force analysis; however, there are indications that the parameters obtained with this model might contain substantial systematic errors (9,10,12,34,55). We compare the kinetic parameters obtained using the Bell-Evans model with the cusp potential model (9). The use of these single-well models is justified below by comparison of the distributions of rupture forces generated by the Bell-Evans model and the distributions generated by a numerical solution of the Fokker-Plank equation using the PMF predicted by molecular dynamics simulations (4,50). The gradual stiffening of the polymeric tethers during pulling is explicitly included in the calculations.

Comparison of the Bell-Evans model to the numerical solution constitutes the first part of the theoretical section. The two-bond rupture model is briefly described in the rest of the theoretical section. In the Results section, we describe the application of the two-bond model to analyze new biotin-streptavidin rupture data. In the Discussion, we compare our results with the kinetic parameters obtained by others; we also demonstrate that if the presence of multiple-bond ruptures is not explicitly considered, the most probable force (MPF) versus log (loading rate) dependence might contain artificial changes in the slope, which may incorrectly be interpreted as additional energy barriers that are not present in the original PMF.

MATERIALS AND METHODS

Sample preparation

Samples were prepared using the previously reported methods (27,34) with slight modification, as indicated below. All chemicals were purchased from Sigma-Aldrich (St. Louis, MO), unless indicated otherwise. Briefly, silicon nitride AFM probes (Veeco, Santa Barbara, CA; model NP) and glass microscope coverslips (Fisher Scientific, Hampton, NH) were cleaned in 2% Hellmanex II (Hellma, Müllheim, Germany) aqueous solution for 3 h. Next, the probes and substrates were rinsed with deionized water (18 M Ω -cm), followed by anhydrous ethanol, then dried under vacuum for 12 h, and transferred into an argon-filled glove box. The probes and substrates were aminated in a saturated ethanolamine hydrochloride solution in anhydrous dimethylsulfoxide for 72 h at room temperature (56). α -N-Hydroxysuccinimide- ω -maleimide-poly(ethylene glycol)-biotin (NHS-PEG-biotin) linkers with a mass-average molecular mass of 3400 Da (Nektar Therapeutics, Huntsville, AL) were covalently attached to the aminated probes through an NHS-amine reaction. This reaction was carried out for 24 h in anhydrous dimethylformamide (DMF) with 5% pyridine (v/v). Next, the probes were reacted with 1900 Da NHS-PEG (Polymer Source, Montreal, Canada) to fill the remaining surface area below the longer PEG tethers.

The shorter PEG was added with the intention of decreasing nonspecific adhesion and pushing the longer tethers away from the surface. This reaction was performed for 48 h in anhydrous DMF with 10% pyridine (v/v). A final reaction with acetic anhydride was performed overnight to block the remaining amines. The probes were then immersed sequentially in preheated hexanes/*i*-propanol (3:2) and water of 50°C–60°C for 1 h. Next, the probes were cleaned successively in toluene, DMF, and ethanol for 15 min each with a platform shaker. Finally, the probes were gently blown dry with ultra high purity nitrogen (National Welders Supply, Charlotte, NC) and used immediately for data collection. The aminated substrates were first activated to

bind amines with a solution of 10 mg of 1,4-phenylenediisothiocyanate (PDITC) (57) in 300 μ l DMF with 5% pyridine (v/v) for 2 h. Next, the slides were cleaned by ultrasonication in DMF and ethanol twice for 10 min each. Then 200 μ l of 100 μ g/ml solution of streptavidin in phosphate buffer saline (PBS, VWR International, West Chester, PA; 0.05 M pH 7 and pH 10 PBS were mixed together to reach pH 8) was deposited on the PDITC-activated substrates. The covalent attachment of streptavidin was performed in a dark environment for 2 h (58). Here, pH 8 PBS solution was chosen to optimize the PDITC-streptavidin reaction (58) while keeping streptavidin stable (59). Finally, the substrates were thoroughly rinsed with pH 7 PBS buffer solution and used immediately for data collection.

Data collection and analysis

Data collection and analysis procedures were similar to those previously reported (29,34). Force spectroscopy experiments were carried out using an Asylum Research (Santa Barbara, CA) MFP-3D AFM. The cantilever spring constants were determined with the built-in thermal noise method (60). All measurements were performed in 0.05 M pH 7 PBS at 20°C. A custom-made temperature stage was used to set the temperature, and a custom-made O-ring was used to reduce evaporation of the PBS when the AFM probe was engaged over the sample. Force curves were collected during the reciprocating probe motion toward and away from the substrate. Simultaneously with the force curve collection, the probe was raster scanned over a $5 \times 5 \mu\text{m}^2$ square area on the substrate (force-volumes with 32×32 lateral size) to obtain a good statistical average. At least 6144 force curves were collected in a series of measurements performed at a given probe velocity. Force curves were collected with 5 nm relative trigger, 0.2 s surface dwell time, and 10 probe velocities ranging from 0.13 to 4 $\mu\text{m/s}$. During the collection of force curves, the probe velocity was cycled from the low to the high value and back several times to distribute possible effects of the probe mechanical wear over the data collected at different velocities.

The control experiments were designed to test the specificity of the measured interactions. Initially, data were collected in a normal fashion as described above with three different probe velocities totaling 8192 force curves at each velocity. The aim here was to measure the detection probability of biotin-streptavidin ruptures under normal conditions. Then 50 μ l of 0.2 mg/ml biotin solution was added to the initial PBS volume of $\sim 200 \mu$ l. The system was allowed to equilibrate for 30 min, and then additional force curves were collected with the same three probe velocities. The change in the detection probability of rupture forces as a result of adding free biotin was measured to verify specificity of the measured rupture forces.

Force-distance curves reveal that the rupture events occur at different probe positions above the sample surface. Before the rupture events, the polymer tethers are stretched with end-to-end distances far exceeding the average distances found at thermal equilibrium. This stretching results in a characteristic force-separation dependence that was used as an initial selection criterion in the data analysis. Rupture events that correspond to the single tether's stretched lengths were used in the statistical analysis of rupture forces. An extended FJC model that includes a conformational transition of PEG linkers (61) was fit to each tether-stretching event provided with the contour lengths and the Kuhn lengths (27). These parameters were used in the subsequent data analysis with the two-bond model that is described below. The data analysis was performed using custom software written for MATLAB (The MathWorks, Natick, MA).

THEORY

Probability density of rupture forces

When a molecular bond is loaded with an increasing external force F , it will eventually rupture, resulting in dissociation of the bound species. According to first-order kinetics, the bond survival probability s as a function of force is given by (4,5)

$$s(F) = \exp \left[- \int_0^F \frac{k(F')}{\dot{F}'} dF' \right]. \quad (1)$$

Here $k(F)$ is the force-dependent dissociation rate and \dot{F} is the loading rate that equals dF/dt . The probability density (PD) function of rupture forces describes the likelihood of rupture at a particular force and is often used to compare the measured distributions of rupture forces to theoretical distributions. The PD function can be calculated by

$$p(F) = - \frac{ds(F)}{dF} = \frac{k(F)}{\dot{F}} s(F). \quad (2)$$

For a sufficiently high loading rate, the PD function often exhibits a maximum (most probable force, MPF) in the range of loading rates accessible by experimental techniques. The dependence of the MPF on the loading rate at the rupture point is commonly used to obtain the kinetic parameters of the dissociation reaction (4,32).

The loading rate (the apparent loading rate) depends on the force sensor (cantilever in AFM experiments) and the polymer tether. The dependence is given by

$$\dot{F} = ((v k_c)^{-1} + l(F)/v)^{-1}. \quad (3)$$

Here, v is the cantilever velocity, F is the force applied to the molecular bond, k_c is the spring constant of the cantilever, $l(F)$ is the force-dependent length of the tether, and prime denotes differentiation with respect to force. In this study we use PEG tethers. The elongation of PEG tethers is calculated by the extended freely jointed chain (eFJC) model (7,61,62). The detailed explanations are included in the Supplementary Material (Data S1).

The dissociation rate is governed by the multidimensional energy landscape that is tilted by the applied force. This landscape is often considered a one-dimensional PMF (4). An analytical formula relating the dissociation rate to the applied force can be obtained for several specific shapes of the potential. The most commonly used are the triangular (Bell-Evans model) (16) and cusp (Hummer-Szabo model) (9) shapes of the bonding potential well with one minimum and one transition state. According to the Bell-Evans model, the dissociation rate depends on applied force as

$$k(F) = k_0 \exp(F x^\ddagger / k_B T). \quad (4)$$

Here k_0 is the dissociation rate at zero applied force, x^\ddagger is the distance between the equilibrium state and the transition state along the dissociation coordinate (henceforth x^\ddagger is called the barrier width for brevity), and $k_B T$ is the thermal energy. For a general shape of the activation barrier, the dissociation rate can be calculated directly without the approximations of Kramer's theory by using the mean first passage time derived from the solution to the Fokker-Plank equation describing stochastic motion in a one-dimensional potential (53). The corresponding dissociation rate is calculated according to (53)

$$k(F)^{-1} = \frac{1}{D} \int_{x_c}^b dx e^{V(x,F)/k_B T} \int_a^x dy e^{-V(y,F)/k_B T}. \quad (5)$$

Here D is the diffusion coefficient, $V(x,F)$ is the PMF tilted by applied load: $V(x,F) = V_0(x) - Fx$; x_c is the position of the minimum in the potential well, and a and b are the positions of the reflecting wall and the sink, respectively. Values for a and b are selected to be sufficiently above and below the transition state and the energy minimum, respectively, as illustrated in Fig. 2. On the right-hand side of Eq. 5 the diffusion coefficient is considered independent of the position along the reaction coordinate. This simplification is justified considering the dominating contribution of exponential terms under the integrals.

The expected PD function in constant-velocity experiments can be calculated by substituting the loading rate from Eq. 3 and the dissociation rate from Eq. 5 into Eqs. 1 and 2. The benefit of this approach is that it allows calculations of the PD directly from the PMF without using the approximations of kinetic theory. This numerical approach is particularly useful when there is no analytical formula for the force dependence of the dissociation rate. In addition, this approach does not assume that the loading rate is constant during pulling. It was shown earlier that these assumptions might result in noticeable systematic errors in the kinetic parameters (32,34,63).

Expected probability density for ruptures of biotin-streptavidin bonds

For ruptures of a biotin-streptavidin bond, the PMF function calculated by molecular dynamics simulations for the biotin-avidin bond (50) has been used previously because of the similarity between the biotin binding pocket in avidin and in streptavidin (16,47). The minimum of the smoothed biotin-avidin PMF is at $\sim -51 k_B T$, whereas the binding free energy of biotin-streptavidin is $\sim 41 k_B T$ (43). Therefore in calculations of the PD for the rupture of the biotin-streptavidin bond, the biotin-avidin PMF was scaled to match the biotin-

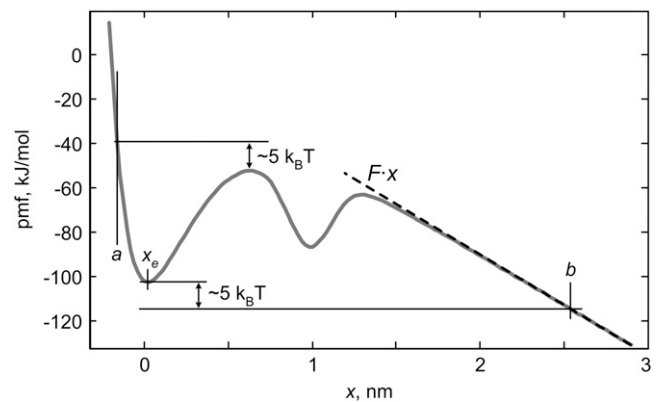


FIGURE 2 The PMF tilted by the applied force. Labels indicate position of the integration limits.

streptavidin binding free energy. The smoothed PMF function was scaled and tilted by the applied force and then substituted into Eq. 5. The diffusion coefficient was selected to be $5 \times 10^{-10} \text{ m}^2/\text{s}$ to approximately match the experimentally measured forces. The loading rate was calculated according to the eFJC model, described in the Supplementary Material (Data S1), with parameters typical in force spectroscopy experiments. The resulting PDs calculated for probe velocities ranging from 1 to 10^5 nm/s are shown in Fig. 3. The inset shows the PMF function that was used to approximate the PMF of the biotin-streptavidin bond. The dashed line in the inset shows the PMF tilted by a force of 60 pN. For forces below $\sim 50 \text{ pN}$, the outer barrier corresponds to the transition state; and for higher forces, the inner barrier (at $\sim 0.6 \text{ nm}$) becomes the transition state. It can be noticed that even with complicated barrier dynamics, the PD functions are represented by a single, well-defined peak without secondary peaks or high-force shoulders.

For a narrower range of probe velocities typical for AFM experiments ($10\text{--}10^4 \text{ nm/s}$) these distributions can be matched reasonably well with distributions calculated according to the Bell-Evans model in Eq. 4 (dashed lines in Fig. 3). The barrier width x^\ddagger that is used in the Bell-Evans model to match the calculations according to the Fokker-Plank equation underestimates the true barrier width by 10%, as indicated by a vertical line in the inset. Also the discrepancy between these models is apparent at the very low probe velocity: the Bell-Evans model predicts higher probability of low rupture forces than the more rigorous calculation by Eq. 5. However these deficiencies of the Bell-Evans model are not significant, and this model will be used for the fitting of the measured histograms of rupture forces according to the model described next.

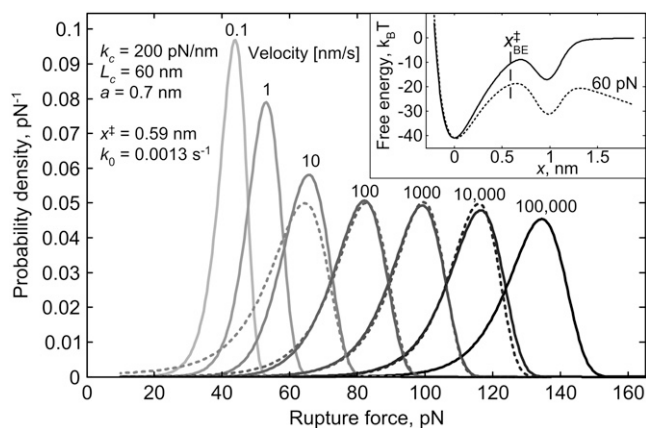


FIGURE 3 Expected PD functions (solid lines) calculated using Eqs. 1–4 and 6 and the PMF from molecular dynamics simulations (shown in the inset) for different probe velocities and parameters given in the graph. Dashed lines show the PD functions calculated using the Bell-Evans kinetic model combined with the eFJC tether model. The kinetic parameters are shown in the graph. The Bell-Evans model calculations were performed for velocities spanning the range available in typical AFM experiments.

Two-bond rupture model

In force spectroscopy experiments, the measured rupture forces may arise not only from single-bond ruptures but also from two-bond ruptures or even multiple-bond ruptures. Because of the low grafting density used in our experiments (34,56) and also for simplicity in the derivations, only two-bond ruptures are considered here. The overall PD of rupture forces can be fit by combining the one- and two-bond rupture PDs according to

$$P_{\text{total}} = A_1 p_1(F) + (1 - A_1) \Pi(F). \quad (6)$$

Here, A_1 is the relative fraction of single-bond rupture events; $p_1(F)$ is the PD of the single-bond ruptures that can be calculated according to Eq. 2; and $\Pi(F)$ is the PD of the two-bond ruptures. An analytical model to calculate this PD is derived in the article by Gu et al. (41). According to this model,

$$\begin{aligned} \Pi(F_\Sigma) \approx & (1 + 2\delta L_c^{\text{max}}) s(F_\Sigma/2) \\ & \times [s(F_2) - s(F_1)] / (F_1 - F_2). \end{aligned} \quad (7)$$

Here $s(F)$ is the single-bond survival probability as a function of force (given by Eq. 1), F_Σ is the total force acting on two bonds (the detected rupture force). The individual forces on bonds are assumed to be acting in the same direction, as illustrated in Fig. 1. The difference between the contour length of two tethers is described by the relative length difference parameter $\delta L_c = (L_{c2} - L_{c1})/L_{c1}$. δL_c^{max} is the maximum δL_c value at which the two ruptures are still detected as a single rupture event. In Eq. 7 forces acting on individual bonds F_1 and F_2 should be evaluated for this maximum relative difference in the tether length. This evaluation requires the solution of the usually transcendental equation that sets the end-to-end distances of two tethers to the same value:

$$l_1(F_1; L_{c1}) = l_2(F_\Sigma - F_1; L_{c1}(1 + \delta L_c)). \quad (8)$$

For a selected tether model and given values of total force F_Σ and contour length difference, Eq. 8 can be solved numerically to obtain F_1 and $F_2 = F_\Sigma - F_1$. For FJC tethers and relatively high forces ($F_\Sigma > 3k_B T/l_K$), Eq. 8 can be solved analytically:

$$\begin{aligned} F_1 = & \frac{F_\Sigma}{2} \\ & + \frac{\sqrt{4F_K F_\Sigma \delta L_c + (F_\Sigma \delta L_c - F_K(2 + \delta L_c))^2 - F_K(2 + \delta L_c)}}{2\delta L_c}. \end{aligned} \quad (9)$$

Here F_K is the characteristic thermal Kuhn force $F_K = k_B T/l_K$. For lower total forces, Eq. 9 underestimates forces F_1 , and at $F_\Sigma = 2F_K$ forces along two tethers become equal to $F_\Sigma/2$. At the low forces the tethers can be considered linear springs and therefore

$$F_1 = F_\Sigma \frac{1 + \delta L_c}{2 + \delta L_c}. \quad (10)$$

The continuous transition from the low to the high-force asymptotics occurs at $\tilde{F}_\Sigma = F_K(2 + \delta L_c)^2 / (1 + \delta L_c)$. Therefore the force F_1 can be estimated using Eq. 10 or Eq. 9 when the total force is below or above the \tilde{F}_Σ limit, respectively. In AFM experiments employing tethers, F_K is usually below 10 pN and therefore this transition force \tilde{F}_Σ is typically below 40 pN. If the measured rupture forces are above \tilde{F}_Σ , the individual forces can be estimated using Eq. 9 alone.

The calculation of the total PD function that includes two bond ruptures requires two additional fit parameters: A_1 and δL_c^{\max} . Here the A_1 parameter determines the amplitude of the single-bond rupture force contribution to the total PD, and δL_c^{\max} parameter determines the relative position of the peak, as demonstrated in Fig. 4. This figure shows the two-bond distributions calculated using parameters typical in AFM experiments. Calculations use the described transition between the low- and high-force limits, and the solution closely matches the solution obtained with numerical calculations of F_1 obtained by solving Eq. 8. With the appropriately selected parameters A_1 and δL_c^{\max} , the distribution of two-bond rupture forces can account for the high-force peak or shoulder that are often obtained in AFM experiments.

RESULTS

Force spectroscopy measurements

Fig. 5 shows typical force plots with biotin-streptavidin molecular bond rupture events preceded by characteristic polymer stretching. Each force plot is characterized by a nonspecific adhesion force peak with varied force height at the sample surface (the tip-sample separation is below 10 nm) and a

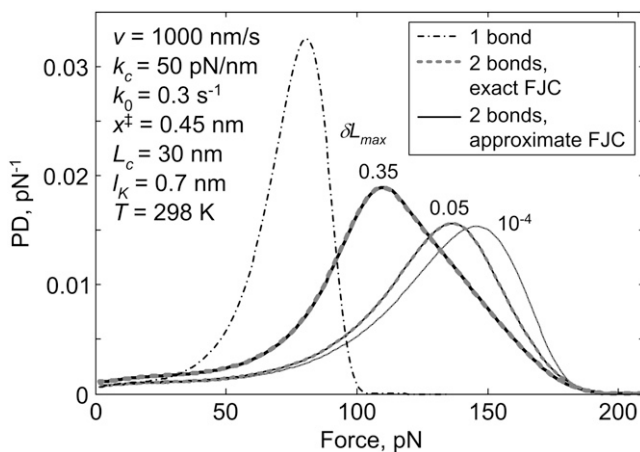


FIGURE 4 PD calculated according to the two-bond rupture model. Calculations use the Bell-Evans kinetic model and the FJC tether model. Other model parameters are shown in the graph. The dash-dotted line shows the single-bond PD. Different values of δL_c^{\max} used in the calculations are shown next to the corresponding lines. Calculations were performed using the numerical solution of Eq. 8 (shaded dashed lines) and by the approximate analytical solution given by Eqs. 9 and 10 (solid black lines). Lines closely overlap, and the difference between numerical and analytical solutions cannot be seen in this graph.

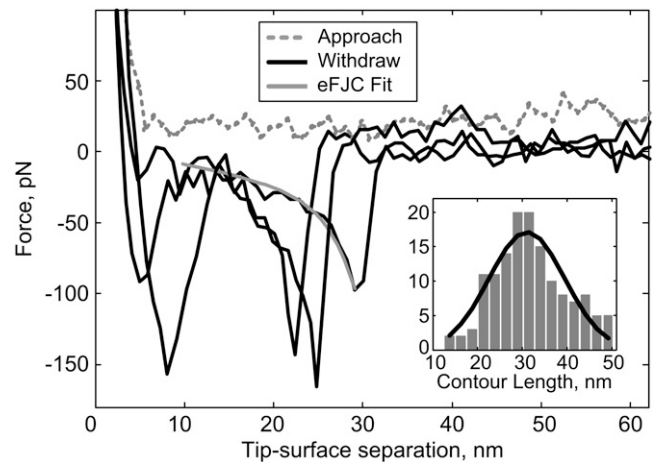


FIGURE 5 Typical force plots exhibiting the rupture events at the tip sample separation that corresponds to the tether length. The fit with the eFJC model to one of the stretching events is also included. The inset shows the contour length distribution obtained from fitting the force curves to the eFJC model.

rupture force peak at the tip-sample separations close to the contour lengths of single polymer PEG tethers (~ 30 nm). The distribution of contour lengths of single tethers extracted from the eFJC fits is shown in the inset. This distribution has a maximum close to the expected value of ~ 30 nm and a significant width. The width of the distribution is attributed to the polydispersity of polymer tethers and the random errors in the fitting of force curves to the eFJC model (34). The rupture events corresponding to the contour lengths from 10 to 50 nm are retained for further analysis. Utilization of tethered biotin excludes nonspecific surface adhesion from the data analysis, facilitating measurements of the desired interactions. The assignment of the measured rupture forces to the biotin-streptavidin interactions is further confirmed by a control experiment in which free biotin molecules are added to the solution to block the interaction sites of streptavidin molecules. The detection probability of the rupture events before adding free biotin is 3.2%. This probability is reduced to 0.7% after adding free biotin molecules. The significant reduction in the detection probability indicates that the specific biotin-streptavidin bonds are ruptured in the experiments (16,45,64).

Of the force curves retained for analysis, $\sim 10\%$ exhibited multiple rupture events in one force curve. In cases when multiple ruptures occurred in the force curve, the last rupture event was analyzed (65).

Fitting histograms of rupture forces

Ten histograms of rupture forces collected at various probe velocities from three individual probe-sample pairs were fit using Eq. 6 with the same kinetic parameters x^\ddagger and k_0 . The maximum relative difference in tether lengths δL_c^{\max} was also allowed to vary during the fit but was kept the same for all histograms. The only fit parameter that varied independently

for each force histogram (apart from different experimental parameters) was the relative amplitude A_1 of the single-bond peak. The limited force sensitivity was accounted for by multiplying the fit function from Eq. 6 by the window function (27,32). The fit minimized the root mean-square (RMS) error calculated as an average RMS error for all histograms. This fitting includes the previously considered effects of the tether stiffening (62,63) and effects of the PMF shape (34). The fitting was performed with the eFJC tether model (29) and two models for the dissociation rate dependence on force: the Bell-Evans and the cusp potential models (12,16). The kinetic parameters obtained with two different kinetic models are listed in Table 1. The errors in parameters were estimated by bootstrapping. In the cusp potential model, the dissociation rate k_0 and the activation energy ΔG^\ddagger are independent parameters. However, because of the relatively narrow range of available velocities, these parameters cannot be independently fit. Therefore, during fitting only the activation energy was varied and the dissociation rate was computed at each step using a constant value of the Arrhenius prefactor A as $k_0 = A \exp(-\Delta G^\ddagger/(k_B T)^{-1})$. The Arrhenius prefactor was kept equal to 10^{11} s^{-1} (47).

Histograms of rupture forces and fits by the Bell-Evans kinetic model are shown in Fig. 6. The contributions from the single and two-bond ruptures are shown with thin dashed and thin solid black lines, respectively. It can be noted that although the data accumulated in Fig. 6 were collected using three different cantilevers with different spring constants ranging from 50 to 160 pN/nm and that the fitting was performed using the same set of kinetic parameters for all histograms, the fit curves match the shape of the histograms quite well. The global fit minimized the average RMS error. Therefore, histograms with fewer data points contributed less significantly to the fit error, though even these histograms are fit well by the model. For several histograms, the fit line goes systematically below the measured values at the high-force end of the fit range. It is possible that in experiments more

than two bonds are ruptured simultaneously and that such ruptures are likely to occur at higher forces. The model includes only the ruptures of two bonds and therefore may not fit well the high-force side of the histogram.

Fit lines that use the cusp model are similar to the Bell-Evans model (the fit errors do not differ significantly for different models; the fit lines are not shown). The cusp potential model gives a larger value for the barrier width than the Bell-Evans model does, similarly to the observation made earlier (33,34). The difference between the barrier widths x^\ddagger for these models (10%) is the same as the difference between the barrier width used in the numerical Fokker-Plank solution and the Bell-Evans model, matching this solution as described in the theoretical section. It appears that an $\sim 10\%$ underestimation error in the barrier width is typical when applying the Bell-Evans model (34). In contrast to the barrier width, the activation energy does not depend significantly on the model.

The maximum relative difference between tether lengths δL_c^{max} obtained from the fits was 0.40 ± 0.06 for the Bell-Evans model and 0.36 ± 0.06 for the cusp model. These values are discussed in the next section.

DISCUSSION

Models accounting for high rupture forces

In this work the presence of the high rupture forces is attributed to the nearly simultaneous rupture of more than one molecular bond (21,67,68). The employed analytical model that describes the rupture of two bonds does not assume that the forces are distributed evenly among the bonds, thus taking into account possible polydispersity in the tether lengths, heterogeneity in the attachment points of molecules to the AFM probe, deviation of the pulling direction from perpendicular to the surface, and sample roughness. The effect of all these factors is combined in a single variable that describes the maximum relative difference in the tether lengths δL_c^{max} . Therefore it is reasonable to suggest that the rather high value of δL_c^{max} obtained from the fits (0.35–0.4) reflects contributions from all other factors and overestimates the tether polydispersity (41).

There are other models that account for the presence of high forces in the distributions. Recently, Pincet and Husson (47) attributed the high forces in the measurements of biotin-streptavidin interactions to the history of the molecular bonds. They suggested that three energy barriers exist in the biotin-streptavidin energy landscape and that higher forces were required to dissociate the old biotin-streptavidin bonds which have been formed for a long time and reached the deepest energy barrier. However, the numerical solution of the Fokker-Plank equation shows no obvious high-force tails even when the activation barrier transfers from the outer to the inner barrier (Fig. 3). Therefore, it appears that the three-barrier model can describe the observed high forces only when the height of the intermediate barrier is specifically selected to reproduce the high forces observed in the distribution.

TABLE 1 Comparison of kinetic parameters from this work and previous results

Reference	x^\ddagger [nm] (inner barrier)	ΔG^\ddagger [kJ·mol ⁻¹] (inner barrier)
This work (Bell-Evans)	0.40 ± 0.05	66.4 ± 1.6
This work (Cusp)	0.44 ± 0.06	66.0 ± 1.6
MD simulation (4,50)	~ 0.5	$\sim 60^*$
(16)	0.12	61^\dagger
(66)	~ 0.22	59^\dagger
(44)	0.05	61^\dagger
(47)	0.31, 0.89	80, 65
(48)	0.024 ± 0.003	$60.0 \pm 60.3^\dagger$
(64)	0.09 ± 0.03	~ 150

*The energy landscape of biotin-streptavidin interaction was scaled to match the binding free energy $\sim 41 k_B T$ (43) based on the energy landscape of the biotin-avidin interaction.

[†]All reference results have been converted by assuming the Arrhenius prefactor to be 10^{11} s^{-1} .

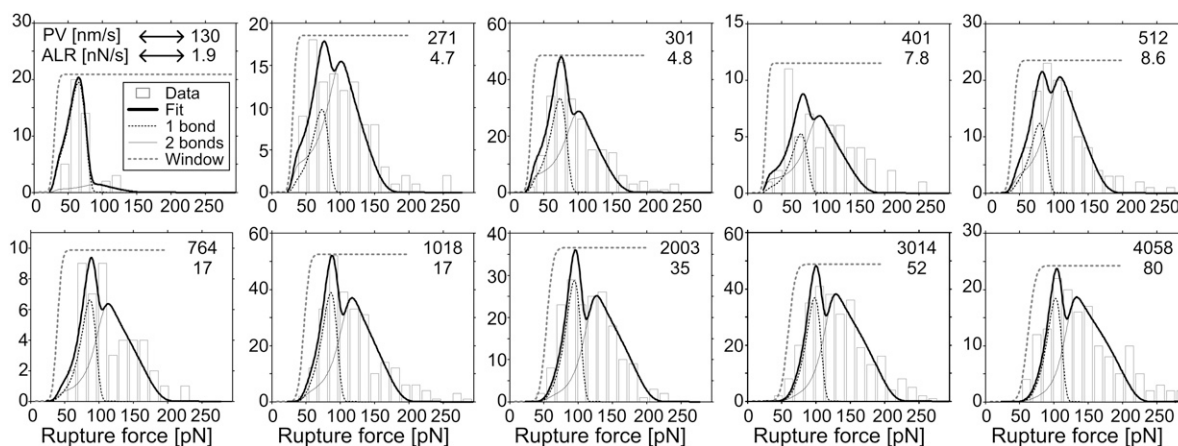


FIGURE 6 Fits of the rupture force histograms by the model given by Eq. 6 that uses the Bell-Evans model for the dissociation rate and the eFJC tether model. Histograms are arranged according to the mean apparent loading rate (ALR) shown in the graphs. The corresponding probe velocities (PV) are also shown in the graphs. The line plots shown in each panel indicate the fit function, the single- and two-bond contributions to the distribution, and the limiting window function. The legend in the top left panel identifies different curves.

The presence of forces that are significantly larger than the MPF in the distribution of rupture forces is not limited to the biotin-streptavidin system but is often observed in many dynamic force spectroscopy experiments involving other interactions (42,51,67,69,70). For a multiple barrier model to explain the high forces observed in these widely different experiments, a specific matching of the height of the inner and intermediate barriers is required. It seems unlikely that such matching would happen for many different molecular bonds. Additionally, the tail of high forces in the distribution is not observed in protein-unfolding experiments that employ tandem protein repeats where the single-molecule nature of the rupture forces is supported by the “signature” rupture pattern (71,72) and in optical tweezers experiments (73). This suggests that in many cases the observed rupture forces depend on the experimental conditions (such as the potential for multiple bond formation) and not on the microscopic details of the PMF.

A more recent model by Raible et al. (51) explains the high-force tail by suggesting a significant heterogeneity in the kinetic parameters that affect the rupture force. The heterogeneity in kinetic parameters required to explain the observed high forces is very large. For instance, the width of the activation barrier has to (in their model) fluctuate from 0 to ~ 1.5 nm, which is unlikely given the size of interacting molecules. Moreover, it might be expected that the fundamental heterogeneity in parameters would manifest itself in all force spectroscopy experiments, but the high forces are not always observed experimentally (as mentioned above). Thus the multiple-bond rupture explanation that depends on the details of experiments is more likely.

Comparison of kinetic parameters

As we discussed in the Theory section, when the pulling force is $> \sim 50$ pN, the inner barrier becomes the transition state. Therefore, because most rupture events measured by AFM

are above 50 pN, the barrier width and activation energy determined by most AFM experiments reflect only the shape of the inner barrier. As shown in Table 1, the barrier width x^\ddagger of the inner barrier measured here is lower than the value from the smoothed PMF predicted by the steered molecular dynamics simulation by $\sim 15\%$ – 25% (4). Despite this inaccuracy, our results are closer to the simulated value in comparison with the results of previous dynamic force spectroscopy measurements. Our activation energy is similar to the height of the inner barrier both from simulation and previous force spectroscopy measurements, given that the error caused by possible uncertainty in the Arrhenius prefactor is ~ 5 kJ \cdot mol $^{-1}$, from ~ 66 kJ \cdot mol $^{-1}$ with a prefactor of 10^{11} s $^{-1}$ to ~ 61 kJ \cdot mol $^{-1}$ with a prefactor of 10^{10} s $^{-1}$ (16).

Ramifications of the multiple-bond ruptures

Partitioning of the rupture force histogram between different components of the two-bond model, as shown in Fig. 6, indicates that ruptures of multiple bonds might widen the force histogram and shift the MPF value to higher forces. Therefore, the multiple-bond rupture events might offset the measured kinetic parameters. However, this is not the only foreseeable consequence of the multiple-bond ruptures. The rupture forces measured by force spectroscopy are often noise limited (32). Therefore if the rupture forces of single bonds fall below the noise threshold, only the ruptures of multiple bonds will contribute to the histograms of rupture forces. In such cases, the apparent MPF will be affected by the noise threshold and the resulting kinetic parameters will not reflect actual bond kinetics. We note that such limitations did not affect the kinetic parameters reported in this work because multiple bonds were explicitly treated in the data analysis.

The force sensitivity in force spectroscopy is usually limited by the cantilever thermal noise with some contribu-

tion of the instrument noise. Typically, force spectroscopy measurements are performed in the frequency range below the fundamental resonance of the cantilever (74). In this frequency range, the cantilever thermal RMS noise is given by (75)

$$\Delta F = \left(\frac{4k_B T \kappa_c B}{\omega_0 Q} \right)^{1/2}. \quad (11)$$

Here $k_B T$ is the thermal energy, κ_c is the cantilever spring constant, B is the detection bandwidth, ω_0 is the angular resonant frequency of the cantilever, and Q is the quality factor. The bandwidth optimal for the detection of rupture events increases with the pulling velocity to preserve the transient details of the force curve (74). Numerical calculations by Kuhner and Gaub indicate that the optimal bandwidth increases in a somewhat piecewise-linear manner with an increase in the pulling velocity. For simplicity in the following analysis, we assume that this dependence is linear. This means that the data are recorded by maintaining the density of data points per displacement distance of the probe: $B = v D_N / 2$, where v is the probe velocity and D_N is the density of the recorded data points per travel distance. Therefore the RMS thermal noise depends on the probe velocity as

$$\Delta F = \left(v \frac{2\kappa_c D_N k_B T}{\omega_0 Q} \right)^{1/2}. \quad (12)$$

The noise limits the detection of the rupture events (76). This limitation can be quantified by the threshold factor of the signal/noise ratio ζ (in the units of RMS noise). The rupture force detection threshold is usually taken at $\zeta = 1$ (76). However, accurate fitting of the force curves by a polymeric tether model and measurements of the apparent loading rate require a higher threshold value. In our experience, the rupture forces should be approximately four times larger than the RMS noise to accurately determine the rupture forces, the mechanical parameters of a polymeric linker, and the apparent loading rate. Thus the noise threshold increases approximately as $v^{1/2}$, and at low velocity values it is typically limited by the DC noise limit. This limit has contributions from the $1/f$ instrument noise and from the noise of measuring the probe position. The most probable rupture force increases approximately logarithmically with the increase of the pulling velocity (7). Given these functional dependencies of rupture force and the noise on the probe velocity, it might be expected that for a particular cantilever there are low and high limits of useful velocities. Outside this detection region, the rupture forces might still be detected; but they would correspond to the ruptures of multiple bonds. Consequently, the measured most probable rupture forces are strongly affected by the velocity-dependent noise threshold outside the useful velocities region.

To illustrate these limitations, force spectroscopy measurements were simulated for probe velocities ranging from

30 to 5000 nm/s. At each velocity, the histogram of rupture forces was generated using Eq. 6 by employing the Bell-Evans kinetics and eFJC tether models. The probability of the single bond detection was kept at 0.6, and the noise threshold was calculated as described above. The resulting histograms were fit by Gaussian curves. The position of the maximum of each Gaussian curve was taken as the apparent MPF. The most probable loading rate was calculated using the tether dynamics model according to Eq. 3. The expected theoretical dependence of the MPF on loading rate was calculated by numerically solving the transcendental equation for the MPF that is derived in Gu et al. (34) (Eq. 2).

The force versus loading rate dependence from the simulated experiment is shown in Fig. 7 A by square symbols, and the theoretical dependence is shown by circles. The other calculation parameters are given in the figure. There are three seemingly linear regions in the simulated force versus $\log(\text{loading rate})$ dependence. Therefore from these data, it might be concluded that there are three barriers to dissociation, although only one barrier was used in the simulation. The slope changes because the noise decreases the detection probability of the single-bond ruptures but still allows the multiple-bond ruptures to be successfully detected. Three rupture force histograms are shown in panels B, C, and D to indicate the origin of a sudden change in the slope.

Three linear regions were fit by the standard Bell-Evans model, which does not take into account tether stiffening. The resulting kinetic parameters are shown in Table 2. It can be noted that neither set of parameters accurately matches the original values used in the calculations. Kinetic parameters at the low and high velocities are significantly altered by the noise threshold. This can be seen by comparing the MPF values extracted by Gaussian fitting and the theoretically expected MPF values. At intermediate velocities, the MPF values obtained by Gaussian fitting are close to the expected theoretical values. Kinetic parameters at these velocities differ from the original parameters mostly because of the tether stiffening effects that were considered previously (32,62,63). Kinetic parameters obtained in this velocity range can be adjusted to obtain more accurate values (62).

The low and high limits for the range of useful velocities can be approximately estimated using the Bell-Evans model by solving the transcendental equation

$$F^\ddagger \ln \left(\frac{\kappa_{\text{eff}} v}{k_0 F^\ddagger} \right) = s \times \left[\frac{v D_N}{2} \left(\frac{4\kappa_c k_B T}{\omega_0 Q} + \Delta F_{\text{white}}^2 \right) + \Delta F_{\text{DC}}^2 \right]^{1/2}. \quad (13)$$

Here κ_{eff} is the effective spring constant (in general, velocity dependent) determined from the cantilever and the tether spring constants as $\kappa_{\text{eff}}^{-1} = \kappa_c^{-1} + \kappa_t^{-1}$, ΔF_{white} is the white noise, ΔF_{DC} is the DC noise, and $F^\ddagger = k_B T / x^\ddagger$. Because the optimal detection bandwidth deviates from the linear dependence that is used in Eq. 12, analytical Eq. 13 gives only approximate estimates of the velocity limits. However, it is

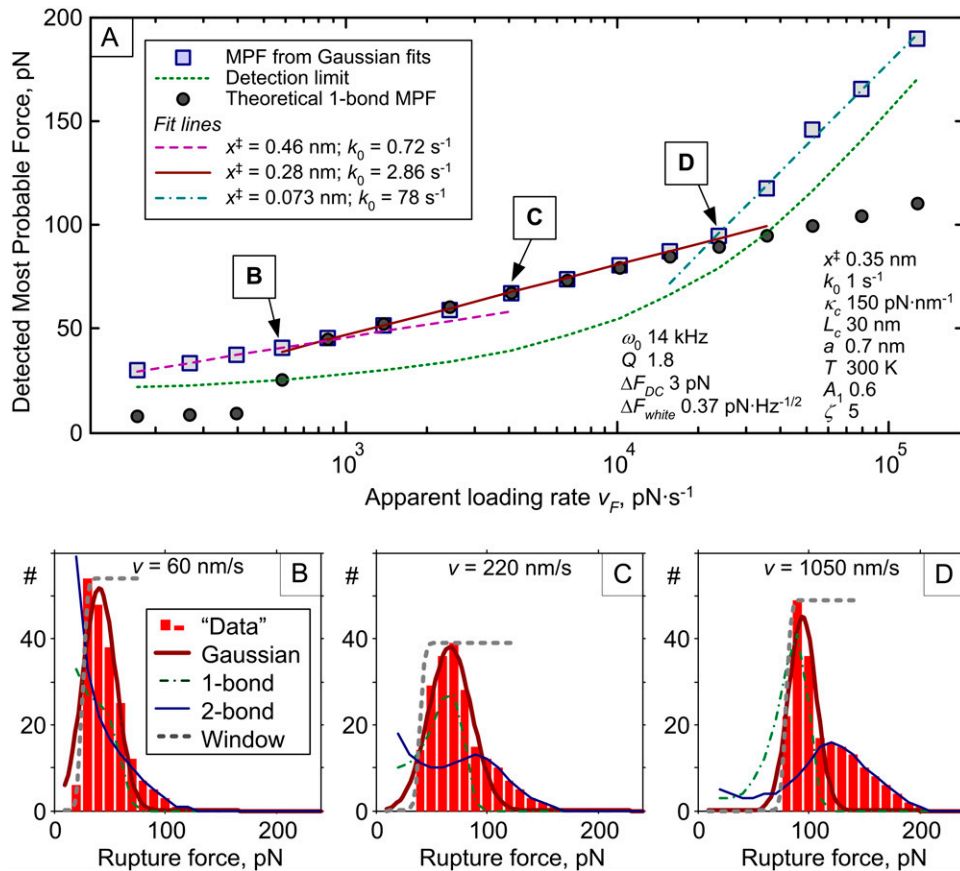


FIGURE 7 (A) MPF versus loading rate dependences from the individual bond rupture model (circles) and from the simulated experiment (squares). Straight lines show fits of the apparent linear regions to the Bell-Evans model. The resulting fit parameters are shown in the legend. (B–D) Calculated histograms of rupture forces at different probe velocities, corresponding to the points indicated in A. Lines show the Gaussian fits, the noise threshold limits, and the one- and two-bond components, as indicated by the legend. Kinetic parameters obtained from the MPF versus loading rate dependence are significantly modified by the noise at the low and high velocities.

instructive to see how the range of useful velocities changes for different experimental parameters.

Fig. 8 shows the velocity limits that were calculated using Eq. 13 for the same set of parameters as in Fig. 7. Panel A shows calculations that assume that κ_t is velocity independent, and in panel B the extended FJC model is used to model the tether stiffening with increasing force (29,61). Calculations show that for relatively high dissociation rates and low tether spring constants there might be no velocity where the most probable rupture force of a single bond is above the noise threshold. In such cases, the multiple-bond ruptures that extend above the noise threshold determine the MPF. Therefore the extracted kinetic parameters might have no clear physical meaning.

Similar calculations can be performed for parameters of a specific force spectroscopy experiment to estimate whether the experiments are performed within velocity limits that allow single-bond rupture detection. We note that even if

experiments are conducted within the range of velocities discussed above, a high probability of the multiple bond formation might still affect the extracted kinetic parameters. Using the two-bond model employed in this work might extend the range of useful velocities. However, at high grafting density, more than two bonds might rupture simultaneously, further complicating the analysis. It was noted previously by Kuhner and Gaub that using polymeric tethers is important for decreasing the effects of the mechanical noise (74). In addition to this benefit, using sparsely grafted polymeric tethers for attaching the sample molecules decreases the probability of multiple bond formation. However, long tethers might be impractical to use because of the noise limitations, as illustrated in Fig. 8 B. The useful velocity ranges depend on the instrument noise and cantilever noise. Decreasing the noise in the experiment to the thermal noise of the cantilever and using small cantilevers can extend the range of the useful velocities to the range limited by the thermal drift on the low side and by the viscous drag on the high side (74,76).

TABLE 2 Kinetic parameters from fitting the apparent linear regions by the Bell-Evans model

	Original parameters	Low velocities	Intermediate velocities	High velocities
x^{\ddagger} [nm]	0.35	0.46	0.28	0.073
k_0 [s^{-1}]	1.0	0.72	2.9	78

CONCLUSIONS

In this article, we considered the effects of possible multiple-bond ruptures on the accuracy of the kinetic parameters measured with force spectroscopy. An approximate analyti-

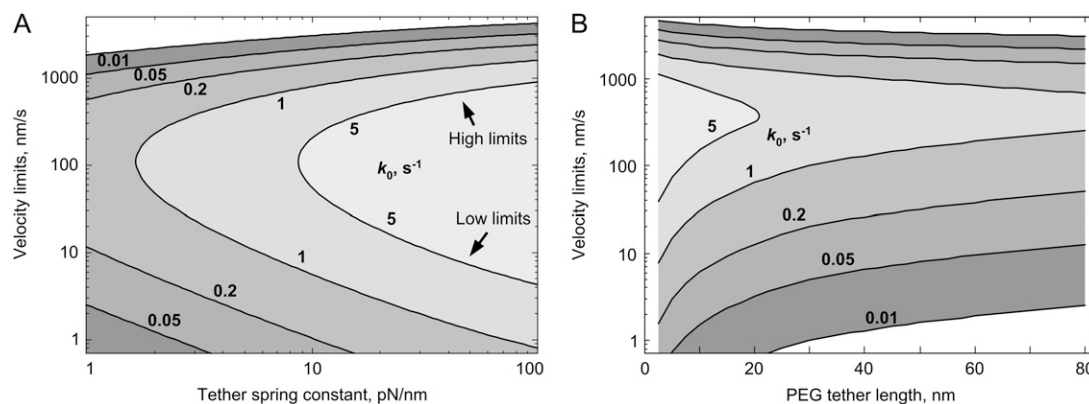


FIGURE 8 Dependence of the velocity limits (A) on the tether stiffness and (B) on the PEG tether length. Calculations performed for several dissociation rates k_0 that are indicated in the corresponding area. Other parameters are the same as in Fig. 7.

cal model that simultaneously considers the ruptures of one and two bonds was applied to analyze the measurements of rupture forces between biotin and streptavidin as well as to compare the resulting kinetic parameters with steered molecular dynamics simulations and with results by others. Analysis indicates that when multiple-bond ruptures are taken into account, the barrier width and the activation energy are close to the values predicted by simulation for the inner barrier of the biotin-streptavidin bond. Additional analysis indicated that the outer barrier was not probed in our AFM-based experiments. It is suggested that the developed model can be widely applied in force spectroscopy experiments that exhibit high forces in the distribution that cannot be explained by models of individual bond rupture.

It is also indicated that in the presence of multiple-bond ruptures the results of force spectroscopy measurements might be affected by the noise. It is shown that at sufficiently low and high probe velocities the rupture force of an individual bond falls below the detection threshold determined by the noise, whereas the ruptures of multiple bonds might still be detected. Therefore outside the window of useful probe velocities the distributions of rupture forces and the extracted MPFs become determined by the noise. Consequently the extracted kinetic parameters might indicate the presence of artificial potential energy barriers. Further analysis indicated that there are experimental conditions in which accurate data reduction based on the MPFs might be impossible. The developed two-bond model is helpful in extending artifact-free analysis to a wider range of probe velocities and to molecular bonds with higher dissociation rates.

SUPPLEMENTARY MATERIAL

To view all of the supplemental files associated with this article, visit www.biophysj.org.

The authors thank Duke University and the National Science Foundation (grant CHE-0719043) for financial support.

REFERENCES

- Bell, G. I. 1978. Models for specific adhesion of cells to cells. *Science*. 200:618–627.
- Baltz, J. M., and R. A. Cone. 1990. The strength of non-covalent biological bonds and adhesions by multiple independent bonds. *J. Theor. Biol.* 142:163–178.
- Leckband, D., and J. Israelachvili. 2001. Intermolecular forces in biology. *Q. Rev. Biophys.* 34:105–267.
- Evans, E., and K. Ritchie. 1997. Dynamic strength of molecular adhesion bonds. *Biophys. J.* 72:1541–1555.
- Garg, A. 1995. Escape-field distribution for escape from a metastable potential well subject to a steadily increasing bias field. *Phys. Rev. B*. 51:15592–15595.
- Evans, E. 1998. Energy landscapes of biomolecular adhesion and receptor anchoring at interfaces explored with dynamic force spectroscopy. *Faraday Discuss.* 111:1–16.
- Evans, E., and K. Ritchie. 1999. Strength of a weak bond connecting flexible polymer chains. *Biophys. J.* 76:2439–2447.
- Heymann, B., and H. Grubmüller. 2000. Dynamic force spectroscopy of molecular adhesion bonds. *Phys. Rev. Lett.* 84:6126–6129.
- Hummer, G., and A. Szabo. 2003. Kinetics from nonequilibrium single-molecule pulling experiments. *Biophys. J.* 85:5–15.
- Dudko, O. K., A. E. Filippov, J. Klafter, and M. Urbakh. 2003. Beyond the conventional description of dynamic force spectroscopy of adhesion bonds. *Proc. Natl. Acad. Sci. USA*. 100:11378–11381.
- Sheng, Y. J., S. Y. Jiang, and H. K. Tsao. 2005. Forced Kramers escape in single-molecule pulling experiments. *J. Chem. Phys.* 123:061106.
- Dudko, O. K., G. Hummer, and A. Szabo. 2006. Intrinsic rates and activation free energies from single-molecule pulling experiments. *Phys. Rev. Lett.* 96:108101.
- Pereverzev, Y. V., and O. V. Prezhdo. 2007. Universal laws in the force-induced unraveling of biological bonds. *Phys. Rev. E Stat. Nonlin. Soft Matter Phys.* 75:011905.
- Rief, M., M. Gautel, F. Oesterhelt, J. M. Fernandez, and H. E. Gaub. 1997. Reversible unfolding of individual titin immunoglobulin domains by AFM. *Science*. 276:1109–1112.
- Fritz, J., A. G. Katopodis, F. Kolbinger, and D. Anselmetti. 1998. Force-mediated kinetics of single P-selectin ligand complexes observed by atomic force microscopy. *Proc. Natl. Acad. Sci. USA*. 95:12283–12288.
- Merkel, R., P. Nassoy, A. Leung, K. Ritchie, and E. Evans. 1999. Energy landscapes of receptor-ligand bonds explored with dynamic force spectroscopy. *Nature*. 397:50–53.
- Li, H. B., A. F. Oberhauser, S. D. Redick, M. Carrion-Vazquez, H. P. Erickson, and J. M. Fernandez. 2001. Multiple conformations of PEVK

- proteins detected by single-molecule techniques. *Proc. Natl. Acad. Sci. USA*. 98:10682–10686.
18. Best, R. B., B. Li, A. Steward, V. Daggett, and J. Clarke. 2001. Can non-mechanical proteins withstand force? Stretching barnase by atomic force microscopy and molecular dynamics simulation. *Biophys. J.* 81:2344–2356.
 19. Brockwell, D. J., G. S. Beddard, E. Paci, D. K. West, P. D. Olmsted, D. A. Smith, and S. E. Radford. 2005. Mechanically unfolding the small, topologically simple protein L. *Biophys. J.* 89:506–519.
 20. Cao, Y., and H. B. Li. 2006. Single molecule force spectroscopy reveals a weakly populated microstate of the FnIII domains of tenascin. *J. Mol. Biol.* 361:372–381.
 21. Florin, E. L., V. T. Moy, and H. E. Gaub. 1994. Adhesion forces between individual ligand-receptor pairs. *Science*. 264:415–417.
 22. Lee, G. U., L. A. Chrisey, and R. J. Colton. 1994. Direct measurement of the forces between complementary strands of DNA. *Science*. 266:771–773.
 23. Bockelmann, U., B. Essevez-Roulet, and F. Heslot. 1998. DNA strand separation studied by single molecule force measurements. *Phys. Rev. E Stat. Phys. Plasmas Fluids Relat. Interdiscip. Topics*. 58:2386–2394.
 24. Rief, M., H. Clausen-Schaumann, and H. E. Gaub. 1999. Sequence-dependent mechanics of single DNA molecules. *Nat. Struct. Biol.* 6:346–349.
 25. Morfill, J., K. Blank, C. Zahnd, B. Luginbuhl, F. Kuhner, K. E. Gottschalk, A. Pluckthun, and H. E. Gaub. 2007. Affinity-matured recombinant antibody fragments analyzed by single-molecule force spectroscopy. *Biophys. J.* 93:3583–3590.
 26. Simson, D. A., M. Strigl, M. Hohenadl, and R. Merkel. 1999. Statistical breakage of single protein A-IgG bonds reveals crossover from spontaneous to force-induced bond dissociation. *Phys. Rev. Lett.* 83:652–655.
 27. Ray, C., and B. B. Akhremitchev. 2005. Conformational heterogeneity of surface-grafted amyloidogenic fragments of alpha-synuclein dimers detected by atomic force microscopy. *J. Am. Chem. Soc.* 127:14739–14744.
 28. McAllister, C., M. A. Karymov, Y. Kawano, A. Y. Lushnikov, A. Mikheikin, V. N. Uversky, and Y. L. Lyubchenko. 2005. Protein interactions and misfolding analyzed by AFM force spectroscopy. *J. Mol. Biol.* 354:1028–1042.
 29. Ray, C., J. R. Brown, and B. B. Akhremitchev. 2006. Single-molecule force spectroscopy measurements of “hydrophobic bond” between tethered hexadecane molecules. *J. Phys. Chem. B*. 110:17578–17583.
 30. Rief, M., J. M. Fernandez, and H. E. Gaub. 1998. Elastically coupled two-level systems as a model for biopolymer extensibility. *Phys. Rev. Lett.* 81:4764–4767.
 31. Kuhner, F., L. T. Costa, P. M. Bisch, S. Thalhammer, W. M. Heckl, and H. E. Gaub. 2004. LexA-DNA bond strength by single molecule force spectroscopy. *Biophys. J.* 87:2683–2690.
 32. Friedsam, C., A. K. Wehle, F. Kuhner, and H. E. Gaub. 2003. Dynamic single-molecule force spectroscopy: bond rupture analysis with variable spacer length. *J. Phys. Condens. Matter*. 15:S1709–S1723.
 33. Wieland, J. A., A. A. Gewirth, and D. E. Leckband. 2005. Single-molecule measurements of the impact of lipid phase behavior on anchor strengths. *J. Phys. Chem. B*. 109:5985–5993.
 34. Gu, C., C. Ray, S. Guo, and B. B. Akhremitchev. 2007. Single-molecule force spectroscopy measurements of interactions between C60 fullerene molecules. *J. Phys. Chem. C*. 111:12898–12905.
 35. Fisher, T. E., P. E. Marszalek, and J. M. Fernandez. 2000. Stretching single molecules into novel conformations using the atomic force microscope. *Nat. Struct. Biol.* 7:719–724.
 36. Snyder, P. W., G. Lee, P. E. Marszalek, R. L. Clark, and E. J. Toone. 2007. A stochastic, cantilever approach to the evaluation of solution phase thermodynamic quantities. *Proc. Natl. Acad. Sci. USA*. 104:2579–2584.
 37. Lo, Y. S., N. D. Huefner, W. S. Chan, F. Stevens, J. M. Harris, and T. P. Beebe. 1999. Specific interactions between biotin and avidin studied by atomic force microscopy using the Poisson statistical analysis method. *Langmuir*. 15:1373–1382.
 38. Ratto, T. V., R. E. Rudd, K. C. Langry, R. L. Balhorn, and M. W. McElfresh. 2006. Nonlinearly additive forces in multivalent ligand binding to a single protein revealed with force spectroscopy. *Langmuir*. 22:1749–1757.
 39. Tees, D. F. J., J. T. Woodward, and D. A. Hammer. 2001. Reliability theory for receptor-ligand bond dissociation. *J. Chem. Phys.* 114:7483–7496.
 40. Williams, P. M. 2003. Analytical descriptions of dynamic force spectroscopy: behaviour of multiple connections. *Anal. Chim. Acta*. 479:107–115.
 41. Gu, C., A. Kirkpatrick, C. Ray, S. Guo, and B. B. Akhremitchev. 2008. Effects of multiple-bond ruptures in force spectroscopy measurements of interactions between fullerene C60 molecules in water. *J. Phys. Chem. C*. 112:5085–5092.
 42. Sulchek, T., R. W. Friddle, and A. Noy. 2006. Strength of multiple parallel biological bonds. *Biophys. J.* 90:4686–4691.
 43. Chilkoti, A., and P. S. Stayton. 1995. Molecular-origins of the slow streptavidin-biotin dissociation kinetics. *J. Am. Chem. Soc.* 117:10622–10628.
 44. Yuan, C. B., A. Chen, P. Kolb, and V. T. Moy. 2000. Energy landscape of streptavidin-biotin complexes measured by atomic force microscopy. *Biochemistry*. 39:10219–10223.
 45. Patel, A. B., S. Allen, M. C. Davies, C. J. Roberts, S. J. B. Tendler, and P. M. Williams. 2004. Influence of architecture on the kinetic stability of molecular assemblies. *J. Am. Chem. Soc.* 126:1318–1319.
 46. Thormann, E., P. L. Hansen, A. C. Simonsen, and O. G. Mouritsen. 2006. Dynamic force spectroscopy on soft molecular systems: improved analysis of unbinding spectra with varying linker compliance. *Colloids Surf. B Biointerfaces*. 53:149–156.
 47. Pincet, F., and J. Husson. 2005. The solution to the streptavidin-biotin paradox: the influence of history on the strength of single molecular bonds. *Biophys. J.* 89:4374–4381.
 48. Piramowicz, M. D., P. Czuba, M. Targosz, K. Burda, and M. Szymonski. 2006. Dynamic force measurements of avidin-biotin and streptavidin-biotin interactions using AFM. *Acta Biochim. Pol.* 53:93–100.
 49. Walton, E. B., S. Lee, and K. J. Van Vliet. 2008. Extending Bell’s model: how force transducer stiffness alters measured unbinding forces and kinetics of molecular complexes. *Biophys. J.* 94:2621–2630.
 50. Izrailev, S., S. Stepaniants, M. Balsera, Y. Oono, and K. Schulten. 1997. Molecular dynamics study of unbinding of the avidin-biotin complex. *Biophys. J.* 72:1568–1581.
 51. Raible, M., M. Evstigneev, F. W. Bartels, R. Eckel, M. Nguyen-Duong, R. Merkel, R. Ros, D. Anselmetti, and P. Reimann. 2006. Theoretical analysis of single-molecule force spectroscopy experiments: heterogeneity of chemical bonds. *Biophys. J.* 90:3851–3864.
 52. Schlierf, M., and M. Rief. 2006. Single-molecule unfolding force distributions reveal a funnel-shaped energy landscape. *Biophys. J.* 90:L33–L35.
 53. Hyeon, C., and D. Thirumalai. 2007. Measuring the energy landscape roughness and the transition state location of biomolecules using single molecule mechanical unfolding experiments. *J. Phys. Condens. Matter*. 19:113101.
 54. Strunz, T., K. Oroszlan, I. Schumakovitch, H. J. Guntherodt, and M. Hegner. 2000. Model energy landscapes and the force-induced dissociation of ligand-receptor bonds. *Biophys. J.* 79:1206–1212.
 55. Hanke, F., and H. J. Kreuzer. 2006. Breaking bonds in the atomic force microscope: theory and analysis. *Phys. Rev. E Stat. Nonlin. Soft Matter Phys.* 74:031909.
 56. Hinterdorfer, P., H. J. Gruber, F. Kienberger, G. Kada, C. Riener, C. Borken, and H. Schindler. 2002. Surface attachment of ligands and receptors for molecular recognition force microscopy. *Colloids Surf. B Biointerfaces*. 23:115–123.
 57. Beier, M., and J. D. Hoheisel. 1999. Versatile derivatisation of solid support media for covalent bonding on DNA-microchips. *Nucleic Acids Res.* 27:1970–1977.

58. Hermanson, G. T. 1996. *Bioconjugate Techniques*. Academic Press, San Diego, CA.
59. Weber, P. C., D. H. Ohlendorf, J. J. Wendoloski, and F. R. Salemme. 1989. Structural origins of high-affinity biotin binding to streptavidin. *Science*. 243:85–88.
60. Proksch, R., T. E. Schäffer, J. P. Cleveland, R. C. Callahan, and M. B. Viani. 2004. Finite optical spot size and position corrections in thermal spring constant calibration. *Nanotechnology*. 15:1344–1350.
61. Oesterhelt, F., M. Rief, and H. E. Gaub. 1999. Single molecule force spectroscopy by AFM indicates helical structure of poly(ethylene-glycol) in water. *N. J. Phys.* 1:6.1–6.11.
62. Ray, C., J. R. Brown, and B. B. Akhremitchev. 2007. Correction of systematic errors in single-molecule force spectroscopy with polymeric tethers by atomic force microscopy. *J. Phys. Chem. B*. 111:1963–1974.
63. Ray, C., J. R. Brown, and B. B. Akhremitchev. 2007. Rupture force analysis and the associated systematic errors in force spectroscopy by AFM. *Langmuir*. 23:6076–6083.
64. Félix Rico, V. T. M. 2007. Energy landscape roughness of the streptavidin-biotin interaction. *J. Mol. Recognit.* 20:495–501.
65. Bemis, J. E., B. B. Akhremitchev, and G. C. Walker. 1999. Single polymer chain elongation by atomic force microscopy. *Langmuir*. 15:2799–2805.
66. Williams, P. M., A. Moore, M. M. Stevens, S. Allen, M. C. Davies, C. J. Roberts, and S. J. B. Tandler. 2000. On the dynamic behaviour of the forced dissociation of ligand-receptor pairs. *J. Chem. Soc. Perkin Trans.* 2:5–8.
67. Kudera, M., C. Eschbaumer, H. E. Gaub, and U. S. Schubert. 2003. Analysis of metallo-supramolecular systems using single-molecule force spectroscopy. *Adv. Funct. Mater.* 13:615–620.
68. Sulchek, T. A., R. W. Friddle, K. Langry, E. Y. Lau, H. Albrecht, T. V. Ratto, S. J. DeNardo, M. E. Colvin, and A. Noy. 2005. Dynamic force spectroscopy of parallel individual Mucin1-antibody bonds. *Proc. Natl. Acad. Sci. USA*. 102:16638–16643.
69. Hukkanen, E. J., J. A. Wieland, A. Gewirth, D. E. Leckband, and R. D. Braatz. 2005. Multiple-bond kinetics from single-molecule pulling experiments: evidence for multiple NCAM bonds. *Biophys. J.* 89:3434–3445.
70. Maki, T., S. Kidoaki, K. Usui, H. Suzuki, M. Ito, F. Ito, Y. Hayashizaki, and T. Matsuda. 2007. Dynamic force spectroscopy of the specific interaction between the PDZ domain and its recognition peptides. *Langmuir*. 23:2668–2673.
71. Schlierf, M., H. B. Li, and J. M. Fernandez. 2004. The unfolding kinetics of ubiquitin captured with single-molecule force-clamp techniques. *Proc. Natl. Acad. Sci. USA*. 101:7299–7304.
72. Cao, Y., and H. B. Li. 2007. Polyprotein of GB1 is an ideal artificial elastomeric protein. *Nat. Mater.* 6:109–114.
73. Kellermyer, M. S. Z., S. B. Smith, C. Bustamante, and H. L. Granzier. 2001. Mechanical fatigue in repetitively stretched single molecules of titin. *Biophys. J.* 80:852–863.
74. Kuhner, F., and H. E. Gaub. 2006. Modelling cantilever-based force spectroscopy with polymers. *Polymer (Guildf.)*. 47:2555–2563.
75. Sarid, D. 1994. *Scanning Force Microscopy*. Oxford University Press, New York.
76. Viani, M. B., T. E. Schaffer, A. Chand, M. Rief, H. E. Gaub, and P. K. Hansma. 1999. Small cantilevers for force spectroscopy of single molecules. *J. Appl. Phys.* 86:2258–2262.